

Chirality Controls Mesenchymal Stem Cell Lineage Diversification through Mechanoresponses

Yan Wei, Shengjie Jiang, Mengting Si, Xuehui Zhang, Jinying Liu, Zheng Wang, Cen Cao, Jianyong Huang, Houbing Huang, Lili Chen, Shutao Wang, Chuanliang Feng,* Xuliang Deng,* and Lei Jiang

Biogenesis and tissue development are based on the heterogenesis of multipotent stem cells. However, the underlying mechanisms of stem cell fate specification are unclear. Chirality is one of the most crucial factors that affects stem cell development and is implicated in asymmetrical cell morphology formation; however, its function in heterogeneous cell fate determination remains elusive. In this study, it is reported that the chirality of a constructed 3D extracellular matrix (ECM) differentiates mesenchymal stem cells to diverse lineages of osteogenic and adipogenic cells by providing primary heterogeneity. Molecular analysis shows that left-handed chirality of the ECM enhances the clustering of the mechanosensor *Itga5*, while right-handed chirality decreases this effect. These differential adhesion patterns further activate distinct mechanotransduction events involving the contractile state, focal adhesion kinase/extracellular signal-regulated kinase 1/2 cascades, and yes-associated protein/runt-related transcription factor 2 nuclear translocation, which direct heterogeneous differentiation. Moreover, theoretical modeling demonstrates that diverse chirality mechanosensing is initiated by biphasic modes of fibronectin tethering. The findings of chirality-dependent lineage specification of stem cells provide potential strategies for the biogenesis of organisms and regenerative therapies.

The establishment of coordinated tissues and organs during biogenesis is one of the most fundamental biological processes, and stem cell heterogenesis plays a crucial role in it.^[1] As an important functional organ that supports the major structures of embryos, the axial skeleton is derived from stem cells located in the paraxial/perisomatic mesoderm.^[2] Furthermore, these cells can also differentiate into other lineages, including adipocytes, dermal cells, and skeletal muscle cells.^[3] Understanding the mechanisms of the heterogenic development of stem cell fate is critical for generating each of these vital structures and elucidating the etiology of congenital diseases.^[4]

Multipotent stem cells in embryos are surrounded by the extracellular matrix (ECM), which provides cells with structural support and environmental cues that influence biological processes. Chirality is one of the earliest heterogenic characteristics of the embryonic ECM.^[5] Increasing

Prof. Y. Wei, Dr. S. Jiang, Dr. M. Si, Prof. X. Deng
Beijing Laboratory of Biomedical Materials
Department of Geriatric Dentistry
Peking University School and Hospital of Stomatology
Beijing 100081, P. R. China
E-mail: kqdengxuliang@bjmu.edu.cn

Prof. X. Zhang
Department of Dental Materials & Dental Medical Devices Testing Center
National Engineering Laboratory for Digital and
Material Technology of Stomatology
Peking University School and Hospital of Stomatology
Beijing 100081, P. R. China

Dr. J. Liu, Prof. C. Feng
State Key Laboratory of Metal Matrix Composite
School of Materials and Science Technology
Shanghai Jiaotong University
Shanghai 200240, P. R. China
E-mail: clfeng@sjtu.edu.cn

Dr. Z. Wang
Department of Physics
University of Science and Technology Beijing
Beijing 100083, P. R. China

Dr. C. Cao, Prof. L. Chen
Department of Stomatology
Union Hospital
Tongji Medical College
Huazhong University of Science and Technology
Wuhan 430022, P. R. China

Prof. J. Huang
Department of Mechanics and Engineering Science
College of Engineering
Peking University
Beijing 100871, P. R. China

Prof. H. Huang
Advanced Research Institute of Multidisciplinary Science
Beijing Institute of Technology
Beijing 100081, P. R. China

Prof. S. Wang, Prof. L. Jiang
CAS Key Laboratory of Bio-inspired Materials and Interfacial Science
CAS Center for Excellence in Nanoscience
Technical Institute of Physics and Chemistry
Chinese Academy of Sciences
Beijing 100190, P. R. China

 The ORCID identification number(s) for the author(s) of this article can be found under <https://doi.org/10.1002/adma.201900582>.

DOI: 10.1002/adma.201900582

evidence has revealed that the molecular chirality modified on a 2D matrix could be converted to a cellular and multicellular asymmetrical structure or motion that finally leads to the disruption of cell morphology symmetry in the plane of the body.^[6] However, these conventional 2D materials could not accurately mimic the biophysical environment of natural 3D ECM. Generally, these matrixes comprise self-assembled chiral-ordered nanofibrous collagen, fibrin, and vitronectin.^[7] These unique chiral nanostructures are capable of encoding sophisticated physiological cell–environment communication by providing high functional group densities and more contact points.^[8] However, the mechanism by which biologically authentic 3D chirality manipulates the heterogenic specification of stem cell fate remains unclear, and this mechanism is challenging to determine. It has been reported that a lack of biomimetic environmental support could compromise the capability of artificial embryos to properly develop into viable organisms.^[9] Therefore, the development of an ECM with chirality would benefit stem cell research. Fundamental insights into the chiral-ordered lineage specification of stem cells might provide the basis for understanding biogenesis and the regeneration of desirable artificial organs in the future.

In this study, we report a potential heterogenesis strategy using 3D ECM-mimetic chirality to control stem cell lineage diversification *in vitro* and *in vivo*. We demonstrated that chirality provided primary heterogeneity to initiate biphasic fibronectin tethering, which induced significant alterations in mechanosensing and mechanotransduction to specify stem cell lineages. This study defines a central regulatory role of chiral cues in modulating stem cell fate with potential translational applications.

To accurately mimic the biophysical environment of natural ECM, amino acids have been considered preferential building blocks because they are fundamental physiological materials, and their chirality determines the higher-order conformations of proteins. Therefore, we used two enantiomers of 4-benzenedicarboxamide phenylalanine derivatives (L-ph and D-ph) to fabricate cell-supporting chiral matrixes by a self-assembly strategy (Figure 1a). The chirality of the matrixes was characterized by circular dichroism (CD) and scanning electron microscopy (SEM). The L-ph and D-ph enantiomers showed CD signals that were equal in intensity and opposite in chirality (Figure S1a, Supporting Information). The representative CD bands of the amide carbonyl groups and the phenyl group in 1,4-benzenedicarboxamide exhibited λ_{\max} values of 218 and 237 nm, respectively. Compared to the enantiomers, the left-handed (LH) and right-handed (DH) matrixes showed a perfect mirror-image relationship, with an increased CD signal intensity and spectral peaks shifted to 226 and 268 nm (Figure S1b, Supporting Information). The racemic (RH) matrix, fabricated by mixing L-ph and D-ph at a molar ratio of 1:1, did not display CD signals. The CD spectra of the LH and DH matrixes (Figure S1c, Supporting Information) during the transformation from gels to solutions displayed a decrease in the signal intensity and reached equilibrium after self-assembly of the enantiomer monomers at 1 h (Figure S1d, Supporting Information). These data indicate that the chirality of the matrixes can be attributed to the self-assembled fibrous aggregates and not to the individual monomers.^[10]

The SEM morphology demonstrated that the LH and DH matrixes were constructed of opposite chiral nanofibers while the RH matrix contained nanofibers without chirality (Figure 1b). These three matrixes presented different chiral nanostructures but almost the same chemical and physical properties, including the diameter (56 ± 13 nm), helical pitch of the nanofibers (510 ± 40 nm), pore size (135 ± 28 μ m), and stiffness (storage modulus $G' \approx 7.5 \times 10^3$ Pa and loss modulus $G'' \approx 3.3 \times 10^3$ Pa) (Figure S1e, Supporting Information). In particular, the helical structure and arrangement of the nanofibers could mimic those of collagen in natural ECM. Therefore, these matrixes allow us to assess the effect of ECM-mimetic chirality on stem cell fate specification in a 3D physiological microenvironment independent of other matrix properties (Figure 1c), which have been linked to cell fate in previous studies.

The diverse differentiation of multipotent stem cells recapitulates the heterogenesis process and represents a valuable platform for studying the mechanisms of cell fate diversification. A live/dead assay (Figure S2a, Supporting Information), a cell counting kit-8 (CCK-8) assay (Figure S2b, Supporting Information), and a CyQUANT assay showed that LH, DH, and RH matrixes had similar biocompatibility to encapsulated mesenchymal stem cells (MSCs). The cell phenotype was analyzed by immunofluorescence chemistry. After incubation for 7 days, runt-related transcription factor 2 (RUNX2) expression was significantly increased in the cells cultured in the LH matrix, while peroxisome proliferator-activated receptor gamma (PPARG) was increased in cells in the DH matrix (Figure 2a). In the RH matrix, staining for RUNX2 and PPARG was mixed and concomitantly observed. The diversity of MSCs lineage specificity was corroborated by an increase in alkaline phosphatase (ALP) production in the LH matrix and an increase in oil red O staining in the DH matrix after 14 days of incubation (Figure 2b). These population differentiation trends were confirmed by counting cells stained for osteogenic (ALP) or adipogenic (lipid) markers and dividing these values by the total number of nuclei (Figure 2c). Osteogenesis was remarkably enhanced in the LH matrix ($68.2 \pm 12.4\%$), while adipogenesis was significantly enhanced in the DH matrix ($46.3 \pm 5.8\%$). These differentiation percentages were comparable to those obtained by chemical induction with osteogenic/adipogenic media.^[11] In addition, reverse transcription polymerase chain reaction (qRT-PCR) (Figure 2d) and Western blotting (Figure 2e) analyses showed that the gene and protein expression of RUNX2, osteocalcin (OCN), and osteopontin (OPN) were increased in the LH matrix, and the gene and protein expression of PPARG and adiponectin (ADN) were obviously upregulated in the DH matrix (Figure 2d).

To gain deeper insight, we performed a global microarray gene analysis. Hierarchical clustering analysis showed that a panel of osteogenic transcripts was upregulated in the LH matrix compared with DH and RH matrixes (Figure 2f; Figure S3a, Supporting Information). In contrast, various adipogenic transcripts were upregulated in the DH matrix compared with the LH and RH matrixes (Figure 2f; Figure S3b, Supporting Information). The in-depth pathway analysis demonstrated that Wnt and transforming growth factor beta (TGF- β) signaling pathways (Figure S3c,d, Supporting Information)

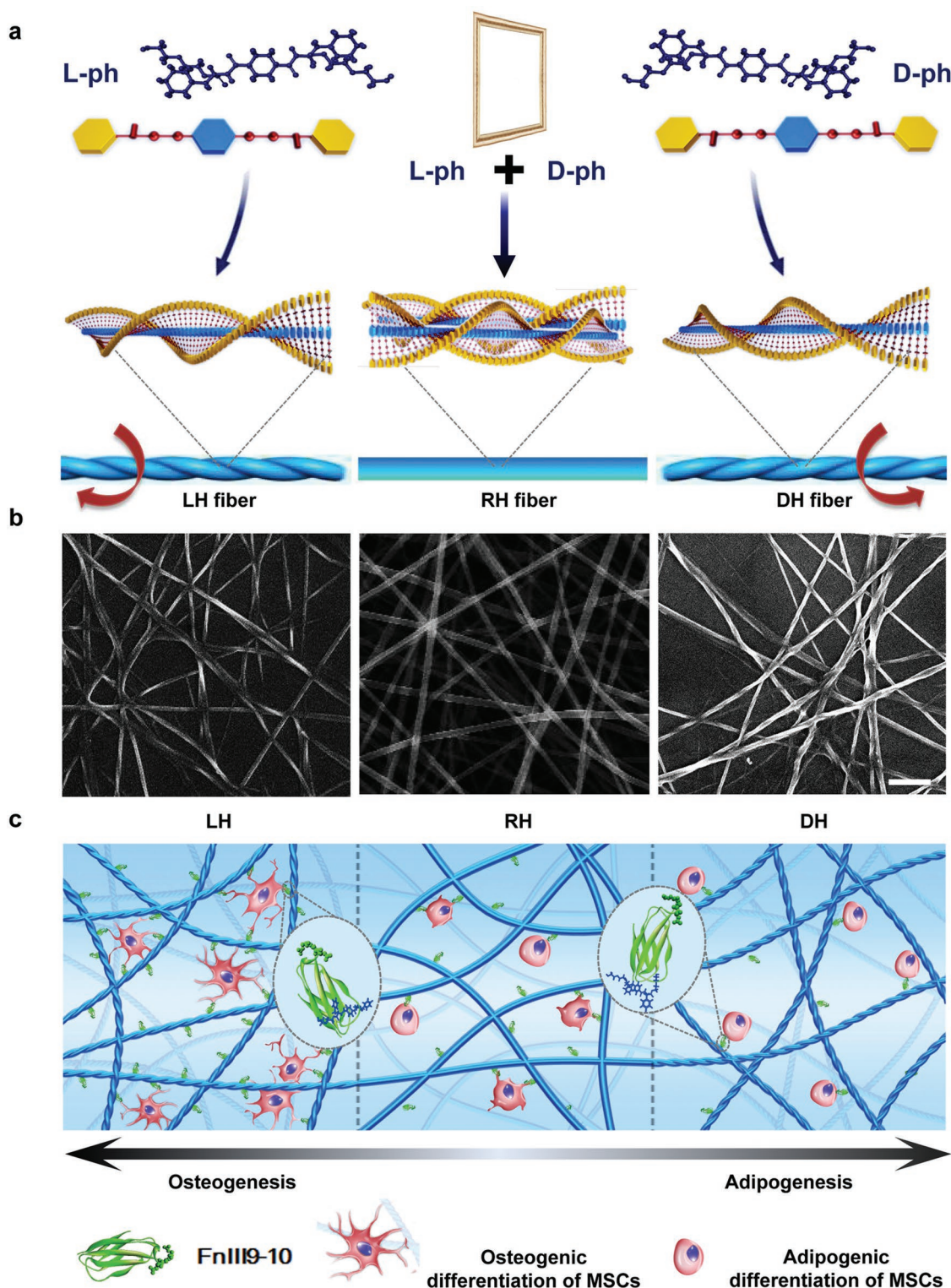


Figure 1. Fabrication of biologically accurate 3D matrixes with tunable chirality. a) A schematic representation of chiral matrix fabrication by the self-assembly of two enantiomers of left-handed 4-benzenedicarboxamide phenylalanine (L-ph) and right-handed 4-benzenedicarboxamide phenylalanine (D-ph) derivatives. b) SEM images of left-handed (LH), right-handed (RH), and racemic (RH) chiral matrixes after freeze-drying. Scale bars: 200 nm. c) A schematic representation of chirality-dependent matrix stem cell fate specification. ECM-mimetic chirality could provide primary heterogeneity to induce biphasic adhesive ligand tethering, which triggers diverse mechanoresponses to distinctly specify MSC osteogenic and adipogenic lineages.

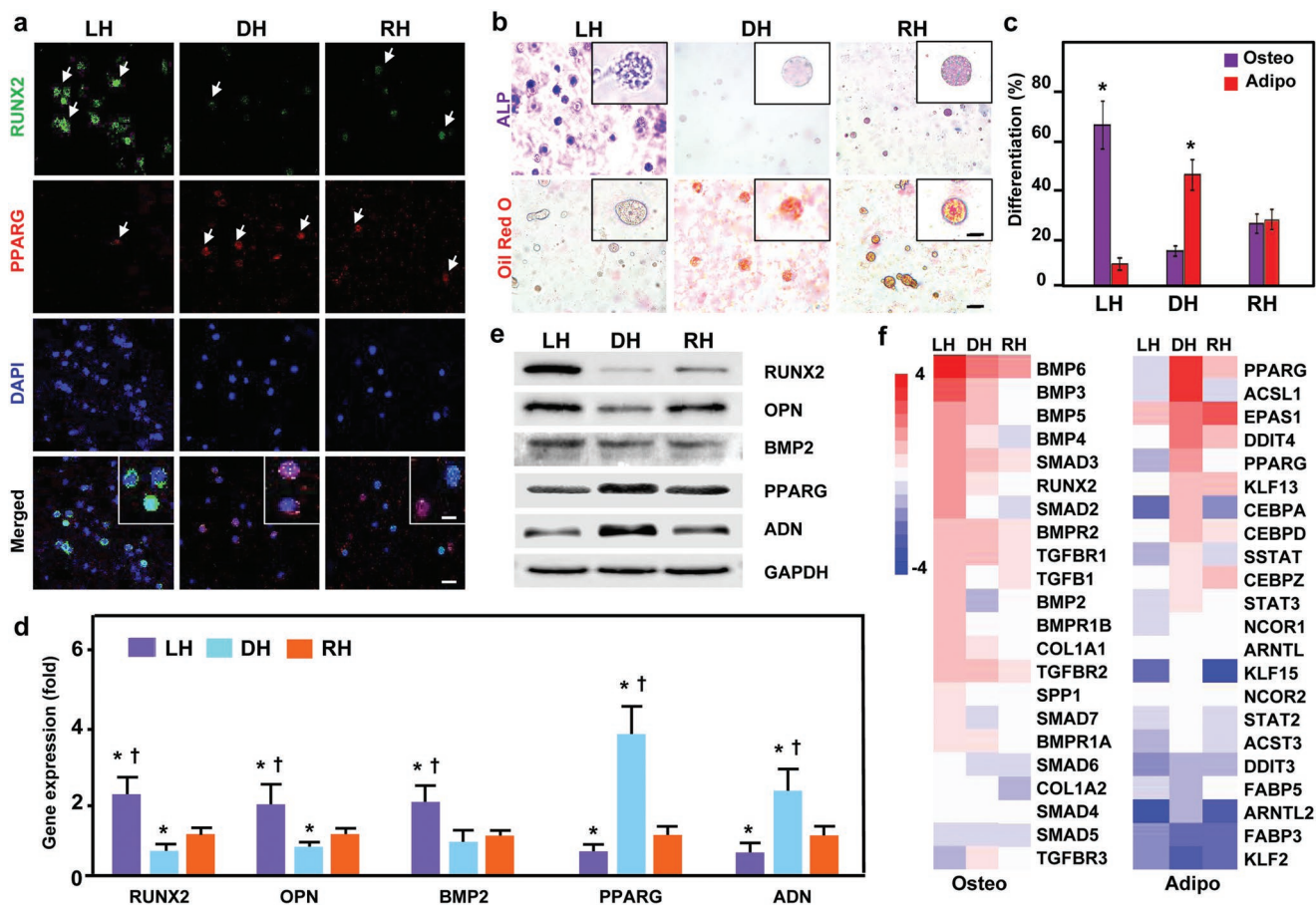


Figure 2. Chirality affects lineage diversification of mesenchymal stem cells (MSCs) in vitro. a) Immunofluorescence staining showing chirality-dependent diverse expression of RUNX2 and PPARG expression. b,c) ALP and lipid droplet staining (b) and the differentiation lineage percentages (c), indicating that the LH matrix obviously enhanced osteogenic lineage commitment, the DH matrix significantly promoted adipogenic lineage commitment, and the RH matrix had no specific effect on cell fate. * $p < 0.05$, *t*-test. d,e) RT-qPCR quantification (d) and Western blotting analysis (e) revealing the greatest upregulation of osteogenic markers (RUNX2, OPN, and bone morphogenetic protein-2 (BMP2)) in the LH matrix and the greatest upregulation of adipogenic markers (PPARG and ADN) in the DH matrix. * $p < 0.05$ versus corresponding RH group, † $p < 0.05$ versus corresponding DH group, one-way analysis of variance (ANOVA) analysis. f) Hierarchical clustering demonstrating that various osteogenic transcripts were upregulated in the LH matrix, while various adipogenic transcripts were upregulated in the DH matrix. Error bars represent standard error of the mean. Scale bars: 30 and 10 μm (insets).

were activated in the LH matrix, while PPAR and adipocytokine signaling pathways were activated triggered in the DH matrix (Figure S3e,f, Supporting Information).

Our data on protein secretion, gene expression, and transcript patterns indicated that the osteogenic commitment of MSCs was promoted in the LH matrix, adipogenesis was favored in the DH matrix, and heterogeneous lineage commitment was observed in the RH matrix. The 3D matrix-mediated MSC lineages were diversified in a moderate microenvironment similar to those in the muscle niche, which is commonly considered to favor myogenesis.^[12] Matrix stiffness has been shown to guide cell fate determination, and a low stiffness is commonly considered to favor adipogenesis.^[13] Therefore, our results identified matrix chirality as a new key regulator of stem cell differentiation and determined it to be as important as bulk stiffness. These 3D ECM-mimetic chirality-mediated diverse lineage preferences are distinct from those previously reported for MSCs cultured on 2D chiral substrates, in which Ding and co-workers found that LH chiral molecules favored

adipogenesis and DH chiral molecules favored osteogenesis.^[14] This difference might be due to the differences between a 2D chiral substrate and a 3D chiral matrix microenvironment, as well as the use of different metrics in their work.

After determining that chiral matrixes can affect MSC lineage commitment specificity in vitro, we next investigated whether combinations of MSCs and chiral matrixes could enhance tissue regeneration in vivo. MSCs in chiral matrixes were injected into freshly formed rat cranial defects covered with nonabsorbable membrane barriers.^[13] MSCs in saline were used as a control. We determined that new bone formed in a chirality-dependent manner. As shown in the microcomputed tomography (μCT) scans (Figure 3a; Figure S4a, Supporting Information), the MSC/LH matrix group showed the greatest amount of new bone formation at all-time points. After 4 weeks, the newly formed bone in the MSC/LH matrix group was distinct, with many regions of bone isolated from host bone tissues, indicating the abundance of multiple centers of new bone formation within the defect area. Fewer isolated

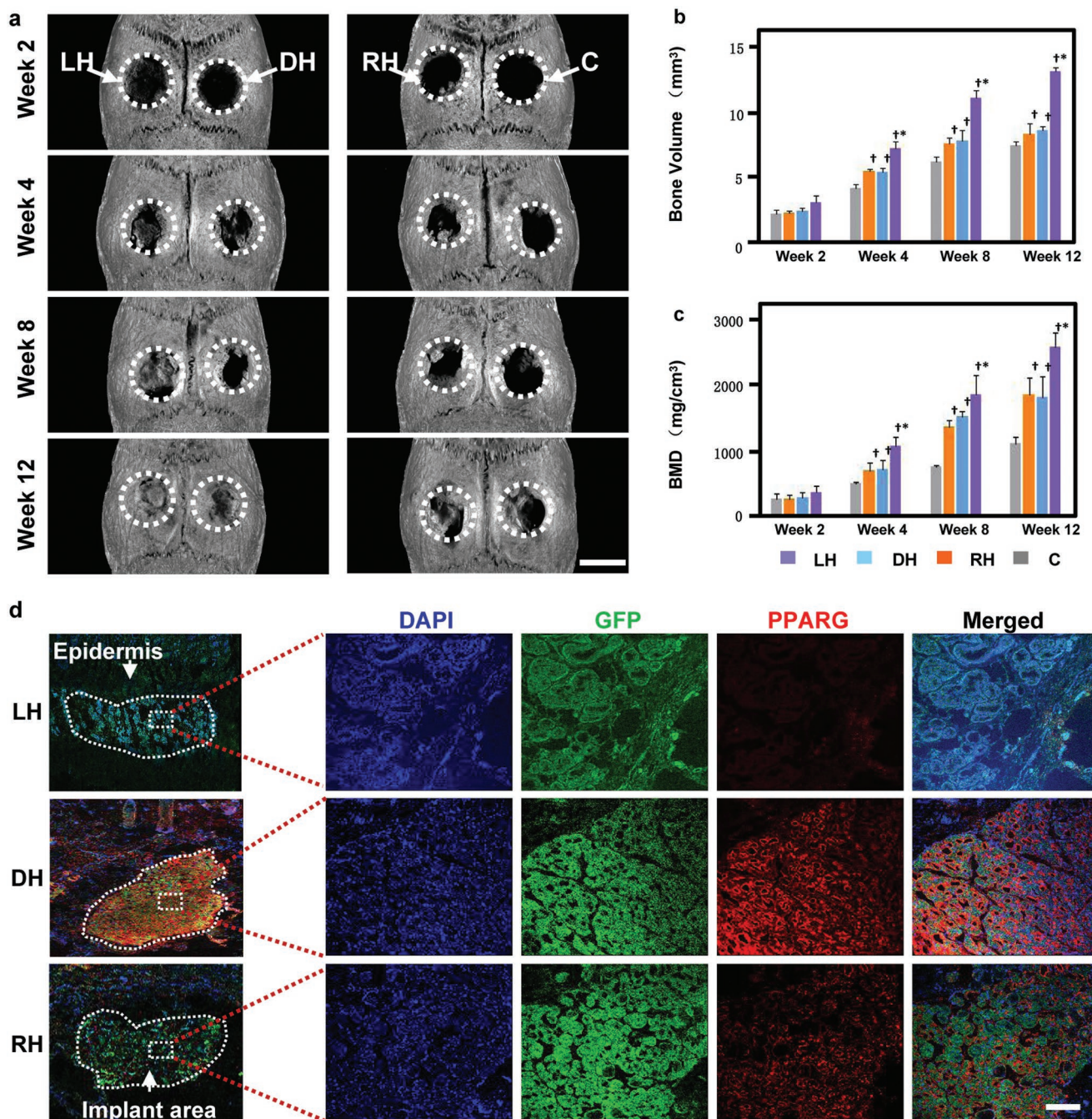


Figure 3. Chirality regulates MSC-mediated tissue regeneration in vivo. a) Representative μ CT images of bone regeneration in rat cranial defects at 2, 4, 8, and 12 weeks after MSC/matrix implantation, showing the most abundant new bone formation in the MSC/LH group. Scale bars: 5 mm. b,c) Quantitative analysis of the total volume (b) and bone mineral density (BMD) (c) of newly formed bone tissue. * $p < 0.05$ versus corresponding RH group, $\dagger p < 0.05$ versus corresponding control group, one-way ANOVA analysis. d) The tracking of MSC-mediated adipogenesis in the subepidermal area of rat axillae 1 week after MSC/matrix implantation, showing that MSCs/DH promoted significantly more PPARG protein expression to facilitate adipogenesis than MSCs/RH and MSCs/LH. Error bars represent standard error of the mean. Scale bars: 0.2 mm.

regions of bone formed after the delivery of MSCs in DH and RH matrixes. In the control group, new bone tissue formed only in the marginal areas of the original bone defect. After 12 weeks, full bone defect repair was observed only in the MSC/LH matrix group. Quantitative analysis (Figure 3b,c) revealed the highest bone volume and bone mineral density (BMD)

values in the MSC/LH matrix group ($p < 0.01$). The MSC/DH and MSC/RH matrix groups showed comparable bone volume and BMD values, while the control group showed the least bone regeneration.

Histological analysis (Figure S4b,c, Supporting Information) with Goldner's trichrome staining revealed that in the MSC/LH

matrix group, a classical trabecular bone structure with an abundance of osteoblasts was present in the bone defect area at 4 weeks, and a mature bone laminate embedded within the bone lacuna was observed after 12 weeks. In the MSC/DH and MSC/RH matrix groups, in addition to less new bone formation, bone maturation was slower than that observed in the MSC/LH matrix group. These findings showed that the LH microenvironment enhances bone tissue regeneration.

To examine the capability of the chiral matrix to enhance adipogenesis *in vivo*, green fluorescent protein (GFP)-tagged MSCs in matrixes were injected into the subepidermal area of rat axillae, which is considered a model of adipose tissue formation.^[15] After 1 week, we found that a significantly higher fluorescence intensity of PPAR γ staining was exhibited in the area of MSC/DH matrix transplantation than in the MSC/RH group (Figure 3c). The least amount of PPAR γ staining within the implant region was observed in the MSCs/LH group. These results showed that the DH matrix displayed a greater ability to support adipogenesis than the RH and LH matrixes. Moreover, immunohistochemistry identified considerable GFP staining within the implant region in all groups, which demonstrated that diverse adipogenesis is mediated by MSCs. These results demonstrate that the LH chiral microenvironment favors osteogenesis and the DH chiral microenvironment favors adipogenesis *in vivo*.

Having established that the 3D chiral microenvironment plays a critical role in regulating MSC fate commitment and tissue regeneration, we investigated how the chiral microenvironment niche affects MSCs. The exact sequence of events and molecular mechanisms leading to chirality-mediated cell fate diversification remains to be elucidated. In this study, we showed a potential role for Itg α 5 in matrix chirality-mediated mechanosensing and heterogenic cell fate commitment. Mounting evidence has defined integrin-mediated adhesion as a central regulator that directly interacts with environmental cues to elicit downstream mechanotransduction events to modulate cellular mechanobiology.^[16] In fact, the functional role of Itg α 5 in the interpretation of 3D matrix properties has been recently characterized, and Itg α 5 binding was identified to be required for osteogenic lineage commitment of stem cells in 3D culture.^[17] In our study, significantly different clustering (Figure 4a; Figure S5a, Supporting Information) and protein production (Figure 4b) of Itg α 5 were found in various chiral matrixes. The enhanced clustering of Itg α 5 was correlated with the promoted expression of osteogenic phenotypic markers and suppressed expression of adipogenic phenotypic markers (Figure 4h). Downregulation of Itg α 5 using specific agents blunted osteogenic differentiation and induced adipogenic differentiation (Figure 4e). These results suggested that matrix chirality and Itg α 5 clustering act in concert to regulate cell fate.

Then, we investigated the potential mechanisms by which Itg α 5 regulates MSC lineage diversification. We showed that a series of mechanotransduction signals were necessary for Itg α 5-induced MSC lineage diversification. Vinculin, an adaptor connecting the intracellular domain of integrin with components of the cytoskeleton,^[18] has often been used as a marker to examine the extent of cellular mechanosensing of the ECM. We found that vinculin staining was obviously increased in the areas of the focal adhesion complexes of

MSCs cultured in LH matrixes compared to those cultured in DH and RH matrixes (Figure S5b, Supporting Information). The cytoskeleton is physically coupled with the focal adhesion complex and nucleus and is considered to play pivotal roles in mechanical signal transduction.^[13,19] By analyzing representative cellular morphology images, we found that MSCs cultured in LH matrixes had a large number of extended cortical protrusions into the surrounding microenvironment after 24 h of culture (Figure 4c), while MSCs in DH and RH matrixes appeared completely spherical with few protrusions (Figure 4c). The highly branched cellular morphology of MSCs cultured in LH matrixes favored osteogenic differentiation, while the spherical MSC morphology favored adipogenesis.^[11,12a] The treatment of cells with cytochalasin D (to inhibit cytoskeletal organization) showed the importance of cytoskeleton organization for increased contractile states (Figure S6a,b, Supporting Information) and osteogenesis, and cytoskeletal inhibition caused decreased contractile states and adipogenesis (Figure S7a,b, Supporting Information). This result is consistent with previous studies that indicated the critical role of cytoskeletal organization in stem cell lineage specification.^[20] These contractile states are known to activate focal adhesion kinase (FAK) and extracellular signal-regulated kinase (ERK) 1/2 signaling (Figure 4b,h), which could further activate SMAD and induce the phosphorylation of RUNX2 to modulate cell fate commitment.^[17] In addition to biochemical molecules, the stretching of organized cytoskeletal fibers can also enlarge nuclear pores to facilitate the nuclear transfer of yes-associated protein (YAP).^[21] After being translocated into the nucleus, YAP acts as a transcription factor regulating subsequent cascades to target gene transcription, triggering cell differentiation.^[22] In our study, the extent of YAP/RUNX2 nuclear translocation was correlated with MSC lineage diversification by gain-of-function (Figure 4d; Figure S8a, Supporting Information) and downregulation studies (Figure S8b, Supporting Information). Moreover, inhibiting Itg α 5 resulted in the overall suppression of these associated mechanotransduction events (Figure 4f–h). Therefore, we propose that the 3D ECM-mimetic chiral microenvironment affects MSC lineage diversification through Itg α 5-initiated mechanosensing and downstream mechanotransduction events, which involve the contractile state, FAK/ERK cascades, and YAP/RUNX2 nuclear translocation (Figure 4i).

But how the above molecular mechanisms were launched in the very first step of cell interpreting matrix chirality? The cell–matrix interactions do not occur directly but through ligand-integrin receptor binding.^[17,23] As Itg α 5 recognition is typically mediated by the RGD sequence of fibronectin (FN), we further characterized the affinity of matrix chirality to FN. The absorption assay showed significantly increased immunofluorescence staining of FN in the LH matrix, which indicated that the LH matrix facilitated an increased amount of ligand adsorption than the DH and RH matrixes (Figure S9a,b, Supporting Information). Increased FN absorption provides an increased amount of RGD sites to facilitate Itg α 5 binding and enhance focal adhesion formation, which affects downstream mechanoresponses and ultimately affects cell fate commitment.^[17] Therefore, our results reveal that the ECM-mimetic chirality could induce diversity in adhesive ligand density, which pave the way to initialize different cellular behavior.

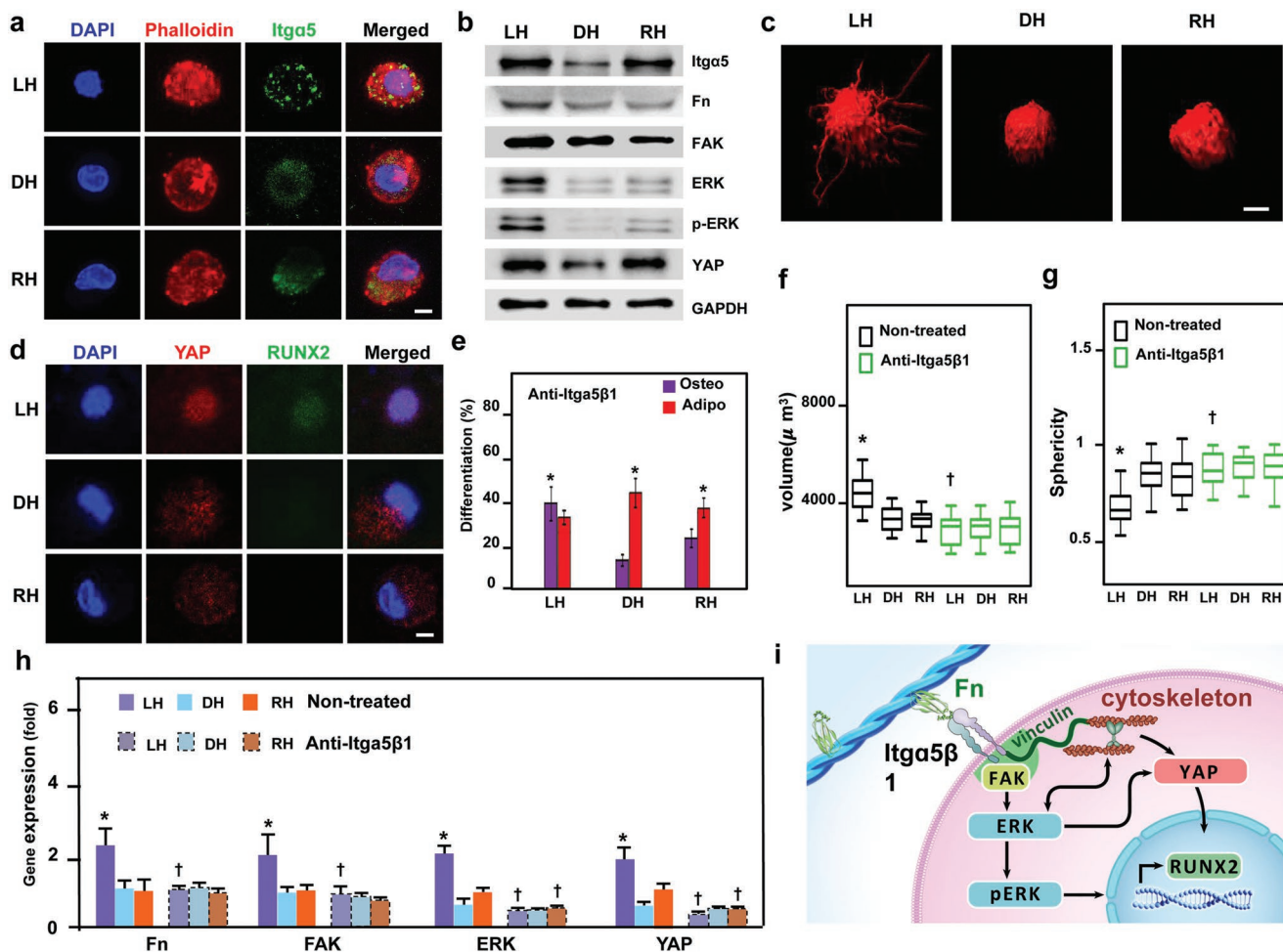


Figure 4. Chirality-dependent activation of the mechanosensor $\text{Itga}5$ -induced diverse downstream mechanotransduction signaling to direct heterogenic differentiation. a) Immunofluorescence analysis showing greater numbers of $\text{Itga}5$ clusters and larger organized $\text{Itga}5$ clusters in LH matrixes than in DH and RH matrixes after 12 h of coculture. Scale bars: 10 μm . b) Western blotting analysis indicating upregulated levels of mechanosensing and mechanotransduction proteins ($\text{Itga}5$, FN, FAK, ERK, pERK, and YAP) in the LH matrix compared with the DH and RH matrixes. c) Representative microscopy images of MSCs cultured in matrixes for 24 h, visualized by F-actin-positive pixel reconstruction (phalloidin, reconstruction (RC)). Scale bars: 5 μm . d) Immunofluorescence staining of YAP and RUNX2 nuclear translocation. Scale bars: 5 μm . e) The inhibition of $\text{Itga}5\beta 1$ activity decreased osteogenic differentiation but enhanced adipogenic differentiation in all matrixes. f,g) The inhibition of $\text{Itga}5\beta 1$ significantly decreased the volume (f) and enhanced the sphericity (g) of MSCs in the LH matrix but only slightly changed these metrics in the DH and RH matrixes. h) RT-qPCR quantification showing significant FAK, ERK, and YAP downregulation after $\text{Itga}5\beta 1$ inhibition. i) A schematic representation of molecular signaling that mediates chiral matrix-induced MSC lineage specificity. * $p < 0.05$ versus the RH group; † $p < 0.05$ versus the corresponding group before inhibiting $\text{Itga}5\beta 1$ (three independent experiments).

But, is the role of ligand density a part of the mechanism or just the mechanism itself? To gain more insight into the initial enantioselectivity between chiral molecules and adhesive ligands, classical molecular dynamic (MD) simulations were performed.^[24] Pioneering studies have showed that FnIII9-10 act as the key cell-binding domains of Fn.^[25] The snapshots showed that L-ph could recognize FnIII9-10 and reach an equilibrium stage within 500 ps, while D-ph could not reach a stable binding site on FnIII9-10 until 1000 ps (Figure 5a; Movies S1 and S2, Supporting Information),^[26] indicating that L-ph had a greater stereoaffinity for FnIII9-10 than that of D-ph. The representative 3D and 2D structures of the adhesive domain complex (Figure 5b) indicate that greater coordination is achieved between L-ph and FnIII9-10 than between D-ph and FnIII9-10. This is presumably a result of the interactions

of greater numbers of residue domains on L-ph than on D-ph (13 domains on L-ph vs 11 domains on D-ph). The quantitative analysis (Figure S9c,d, Supporting Information) further demonstrated the narrower distribution of the binding pair distance in the L-ph-FnIII9-10 complex (1.6 ± 0.8 nm) than in the D-ph-FnIII9-10 complex (2.1 ± 0.9 nm). This high stereoaffinity of L-ph for FnIII9-10 was also supported by the lower total interaction energy, van der Waals interaction energy and H-bond interaction energy of the L-ph-FnIII9-10 complex (Figure 5c). Overall, the classical MD simulations revealed that faster recognition, increased stereoaffinity, enhanced coordination, and lower binding energy were achieved between L-ph and FnIII9-10 than between D-ph and FnIII9-10. According to the ECM tethering theory, these alterations in anchoring points and adhesive distance may induce local stiffness modifications,

for D-ph, Figure 5d) and root-mean-square fluctuation (RMSF) (12.2×10^{-3} for L-ph vs 9.8×10^{-3} for D-ph, Figure 5e) values for RGD indicated that the high interdomain elasticity and flexibility of the RGD configuration in the L-ph-FnIII9-10 complex could facilitate integrin binding to the initial downstream cell response.^[28] These data demonstrate that ECM-mimetic 3D chirality could enantioselectively manipulate ligand tethering pattern in both ligand density and RGD configuration.

To test the modality of the enantioselectivity indicated by the MD simulation, we investigated the stability of MSC aggregates on chiral matrixes.^[29] We observed that cells exhibited the fastest escape from aggregates on the LH matrix and formed disconnected cell aggregates (Figure S10a, Supporting Information). The quantified cell spreading kinetics over time (Figure S10b, Supporting Information) demonstrated enhanced cell spreading on the LH matrix. The cell-spreading rate was considered to be dominantly influenced by the adhesive ligand adsorbed to the matrixes. Compared with DH and RH matrixes, the LH matrix demonstrated increased adhesive ligand affinity and provided a greater number of integrin binding sites, resulting in faster cell motility. Therefore, our data indicate that chirality could provide primary heterogeneity to induce biphasic adhesive ligand tethering, thus linking the subsequent onset of chirality-mediated diverse signaling events and lineage specificity.

In conclusion, by simply tuning the matrix chirality, we precisely controlled stem cell lineage diversification with a high efficiency comparable to that of classical chemical induction. This strategy depends only on the matrix chirality and avoids multiple chemical modifications of the ECM, in which hydrogels must be cross-linked by polymerization to achieve certain stiffness. Our findings of chirality-dependent lineage specification of stem cells provide a practical, simple, and efficient strategy for directing biogenesis and regeneration.

Supporting Information

Supporting Information is available from the Wiley Online Library or from the author.

Acknowledgements

Y.W., S.J., M.S., and X.Z. contributed equally to this work. The authors thank Prof. Ce-Wen Nan from Tsinghua University for valuable suggestions. This work was supported by the National Key R&D Program of China (2018YFC1105301, 2018YFC1105302, 2018YFC1105303, 2018YFC1105304, and 2017YFC1104302), the National Natural Science Foundation of China (81425007, 31570990, 51833006, 51772006, 31670993, and 21425314), the Fok Ying Tong Education Foundation (151034), and the Innovation Program of Shanghai Municipal Education Commission (201701070002E00061). All animal experiments were conducted with the approval of the Animal Care and Use Committee of Peking University (IACUC number: LA2018246).

Conflict of Interest

The authors declare no conflict of interest.

Keywords

cellular mechanics, lineage diversification, matrix chirality

Received: January 24, 2019
Published online: March 5, 2019

- [1] a) G. Cossu, M. Birchall, T. Brown, P. De Coppi, E. Culme-Seymour, S. Gibbon, J. Hitchcock, C. Mason, J. Montgomery, S. Morris, F. Muntoni, D. Napier, N. Owji, A. Prasad, J. Round, P. Saprui, J. Stilgoe, A. Thrasher, J. Wilson, *Lancet* **2018**, *391*, 883; b) M. Guo, A. F. Pegoraro, A. Mao, E. H. Zhou, P. R. Arany, Y. Han, D. T. Burnette, M. H. Jensen, K. E. Kasza, J. R. Moore, F. C. Mackintosh, J. J. Fredberg, D. J. Mooney, J. Lippincott-Schwartz, D. A. Weitz, *Natl. Acad. Sci. USA* **2017**, *114*, 201705179.
- [2] A. I. Caplan, D. Correa, *Cell Stem Cell* **2011**, *9*, 11.
- [3] a) B. Trappmann, J. E. Gautrot, J. T. Connelly, D. G. T. Strange, Y. Li, M. L. Oyen, M. A. Cohen Stuart, H. Boehm, B. Li, V. Vogel, J. P. Spatz, F. M. Watt, W. T. S. Huck, *Nat. Mater.* **2012**, *11*, 642; b) T. H. Ambrosi, A. Scialdone, A. Graja, S. Gohlke, A. M. Jank, C. Bocian, L. Woelk, H. Fan, D. W. Logan, A. Schürmann, L. R. Saraiva, T. J. Schulz, *Cell Stem Cell* **2017**, *20*, 771.
- [4] a) R. Sanalkumar, K. D. Johnson, X. Gao, M. E. Boyer, Y.-I. Chang, K. J. Hewitt, J. Zhang, E. H. Bresnick, *Proc. Natl. Acad. Sci. USA* **2014**, *111*, E1091; b) R. Nusse, H. Clevers, *Cell* **2017**, *169*, 985.
- [5] a) E. Yashima, N. Ousaka, D. Taura, K. Shimomura, T. Ikai, K. Maeda, *Chem. Rev.* **2016**, *116*, 13752; b) S. M. Morrow, A. J. Bissette, S. P. Fletcher, *Nat. Nanotechnol.* **2017**, *12*, 410; c) J. E. Hein, D. G. Blackmond, *Acc. Chem. Res.* **2012**, *45*, 2045; d) M. Liu, L. Zhang, T. Wang, *Chem. Rev.* **2015**, *115*, 7304; e) Y. H. Tee, T. Shemesh, V. Thiagarajan, R. F. Hariadi, K. L. Anderson, C. Page, N. Volkmann, D. Hanein, S. Sivaramakrishnan, M. M. Kozlov, A. D. Bershadsky, *Nat. Cell Biol.* **2015**, *17*, 445.
- [6] a) K. Lv, L. Zhang, W. Lu, M. Liu, *ACS Appl. Mater. Interfaces* **2014**, *6*, 18878; b) K. Taniguchi, R. Maeda, T. Ando, T. Okumura, N. Nakazawa, R. Hatori, M. Nakamura, S. Hozumi, H. Fujiwara, K. Matsuno, *Adv. Healthcare Mater.* **2011**, *333*, 339; c) X. Zhao, L. Xu, M. Sun, W. Ma, X. Wu, C. Xu, H. Kuang, *Nat. Commun.* **2017**, *8*, 2007; d) J. Deng, H. Zheng, X. Zheng, M. Yao, Z. Li, C. Gao, *Nano Res.* **2016**, *9*, 3683.
- [7] a) X.-Q. Dou, C.-L. Feng, *Adv. Mater.* **2017**, *29*, 1604062; b) J. Thiele, Y. Ma, S. M. C. Bruekers, S. Ma, W. T. S. Huck, *Adv. Mater.* **2014**, *26*, 125.
- [8] a) L. Pérez-García, D. B. Amabilino, *Chem. Soc. Rev.* **2007**, *36*, 941; b) G. A. Hembury, V. V. Borovkov, Y. Inoue, *Chem. Rev.* **2008**, *108*, 1; c) J. Zhou, J. Li, X. Du, B. Xu, *Biomaterials* **2017**, *129*, 1.
- [9] S. E. Harrison, B. Sozen, M. Zernicka-Goetz, *Nat. Protoc.* **2018**, *13*, 1586.
- [10] D. Yang, P. Duan, L. Zhang, M. Liu, *Nat. Commun.* **2017**, *8*, 1.
- [11] a) S. Khetan, M. Guvendiren, W. R. Legant, D. M. Cohen, C. S. Chen, J. A. Burdick, *Nat. Mater.* **2013**, *12*, 458. b) M. Bao, J. Xie, A. Piruska, W. T. S. Huck, *Nat. Commun.* **2017**, *8*, 1.
- [12] a) O. Chaudhuri, L. Gu, D. Klumpers, M. Darnell, S. A. Bencherif, J. C. Weaver, N. Huebsch, H. P. Lee, E. Lippens, G. N. Duda, D. J. Mooney, *Nat. Mater.* **2016**, *15*, 326. b) A. J. Engler, S. Sen, H. L. Sweeney, D. E. Discher, *Cell* **2006**, *126*, 677.
- [13] N. Huebsch, E. Lippens, K. Lee, M. Mehta, S. T. Koshy, M. C. Darnell, R. M. Desai, C. M. Madl, M. Xu, X. Zhao, O. Chaudhuri, C. Verbeke, W. S. Kim, K. Alim, A. Mammoto, D. E. Ingber, G. N. Duda, D. J. Mooney, *Nat. Mater.* **2015**, *14*, 1269.
- [14] X. Yao, Y. Hu, B. Cao, R. Peng, J. Ding, *Biomaterials* **2013**, *34*, 9001.
- [15] T. T. Y. Han, S. Toutounji, B. G. Amsden, L. E. Flynn, *Biomaterials* **2015**, *72*, 125.

- [16] a) M. J. Dalby, N. Gadegaard, R. O. C. Oreffo, *Nat. Mater.* **2014**, *13*, 558; b) S. Cho, J. Irianto, D. E. Discher, *J. Cell Biol.* **2017**, *216*, 305.
- [17] Z. Hamidouche, O. Fromigue, J. Ringe, T. Haupl, P. Vaudin, J.-C. Pages, S. Srouji, E. Livne, P. J. Marie, *Proc. Natl. Acad. Sci. USA* **2009**, *106*, 18587.
- [18] a) A. Elosegui-Artola, R. Oria, Y. Chen, A. Kosmalka, C. Pérez-González, N. Castro, C. Zhu, X. Trepal, P. Roca-Cusachs, *Nat. Cell Biol.* **2016**, *18*, 540; b) J. D. Humphrey, E. R. Dufresne, M. A. Schwartz, *Nat. Rev. Mol. Cell Biol.* **2014**, *15*, 802.
- [19] A. Tajik, Y. Zhang, F. Wei, J. Sun, Q. Jia, W. Zhou, R. Singh, N. Khanna, A. S. Belmont, N. Wang, *Nat. Mater.* **2016**, *15*, 1287.
- [20] T. C. Von Erlach, S. Bertazzo, M. A. Wozniak, C. M. Horejs, S. A. Maynard, S. Attwood, B. K. Robinson, H. Autefage, C. Kallepitis, A. Del Río Hernández, C. S. Chen, S. Goldoni, M. M. Stevens, *Nat. Mater.* **2018**, *17*, 237.
- [21] Z. Meng, Y. Qiu, K. C. Lin, A. Kumar, J. K. Placone, C. Fang, K.-C. Wang, S. Lu, M. Pan, A. W. Hong, T. Moroishi, M. Luo, S. W. Plouffe, Y. Diao, Z. Ye, H. W. Park, X. Wang, F.-X. Yu, S. Chien, C.-Y. Wang, B. Ren, A. J. Engler, K.-L. Guan, *Nature* **2018**, *560*, 655.
- [22] S. Dupont, L. Morsut, M. Aragona, E. Enzo, S. Giulitti, M. Cordenonsi, F. Zanconato, J. Le Dıgabel, M. Forcato, S. Bicciato, N. Elvassore, S. Piccolo, *Nature* **2011**, *474*, 179.
- [23] R. K. Das, O. F. Zouani, C. Labrugère, R. Oda, M. C. Durrieu, *ACS Nano* **2013**, *7*, 3351.
- [24] a) G. Raffaini, F. Ganazzoli, *Langmuir* **2004**, *20*, 3371; b) C. Liao, Y. Xie, J. Zhou, *RSC Adv.* **2014**, *4*, 15759.
- [25] A. M. D. Wan, R. M. Schur, C. K. Ober, C. Fischbach, D. Gourdon, G. G. Malliaras, *Adv. Mater.* **2012**, *24*, 2501.
- [26] J. E. Stone, A. P. Hynninen, J. C. Phillips, K. Schulten, *Lect. Notes Comput. Sci.* **2016**, 9945, 188.
- [27] A. Paladino, M. Civera, L. Belvisi, G. Colombo, *PLoS Comput. Biol.* **2017**, *13*, e1005334.
- [28] H. J. Huang, T. T. Chang, H. Y. Chen, C. Y. C. Chen, *Evidence-Based Complement. Altern. Med.* **2014**, 2014, 1.
- [29] S. Douezan, K. Guevorkian, R. Naouar, S. Dufour, D. Cuvelier, F. Brochard-Wyart, *Proc. Natl. Acad. Sci. USA* **2011**, *108*, 7315.